RAPID COMMUNICATION

Dynamic modeling of total ionizing dose-induced threshold voltage shifts in MOS devices

Guangbao Lu(陆广宝)[1,2,†], Jun Liu(刘俊)[1,2,†], Chuanguo Zhang(张传国)[1], Yang Gao(高扬)[1,2], and Yonggang Li(李永钢)[1,2,‡]

[1] *Key Laboratory of Materials Physics, Institute of Solid State Physics, HFIPS, Chinese Academy of Sciences, Hefei* 230031, *China*
[2] *University of Science and Technology of China, Hefei* 230026, *China*

(Received 26 August 2022; revised manuscript received 31 October 2022; accepted manuscript online 3 November 2022)

The total ionizing dose (TID) effect is a key cause for the degradation/failure of semiconductor device performance under energetic-particle irradiation. We developed a dynamic model of mobile particles and defects by solving the rate equations and Poisson's equation simultaneously, to understand threshold voltage shifts induced by TID in silicon-based metal–oxide–semiconductor (MOS) devices. The calculated charged defect distribution and corresponding electric field under different TIDs are consistent with experiments. TID changes the electric field at the Si/SiO_2 interface by inducing the accumulation of oxide charged defects nearby, thus shifting the threshold voltage accordingly. With increasing TID, the oxide charged defects increase to saturation, and the electric field increases following the universal 2/3 power law. Through analyzing the influence of TID on the interfacial electric field by different factors, we recommend that the radiation-hardened performance of devices can be improved by choosing a thin oxide layer with high permittivity and under high gate voltages.

Keywords: dynamic modeling, total ionizing dose, threshold voltage shifts, radiation-hardening

PACS: 85.30.–z, 85.30.De, 24.10.–i, 42.88.+h **DOI:** 10.1088/1674-1056/ac9fc4

1. Introduction

Silicon-based semiconductor devices are widely-served in the extreme irradiation environments of the aviation and nuclear industries. Irradiation of high-energy rays is one of the main reasons for metal–oxide–semiconductor (MOS) device performance degradation/failure.[1,2] The irradiation effects of MOS devices are mainly divided into displacement and ionizing damage.[3] In particular, ionizing damage is caused by electron excitation to induce electron–hole (e-h) pairs when high-energy particles (such as photons or electrons) pass through the materials. There are two basic effects of ionizing damage, that is, the total ionizing dose (TID) and single event effects, caused by the cumulative effect of high-energy particles[4] and the transient effect of a single high-energy particle,[5] respectively. The TID effect is the main cause of ionizing damage to MOS devices, such as low threshold voltage, low channel mobility, high leakage current, high on-resistance, low breakdown voltage, and electroluminescence.[6–9] Among them, the threshold voltage shift ($\Delta V_{\rm th}$) can cause the permanent failure of devices, which is a major unresolved issue that is sensitive to TID.[10]

The failure of the communication satellite Telstar I in 1963 prompted researchers to study the effects of ionizing radiation.[11] In 1964, Hughes and Giroux conducted the first experimental study on the degradation of MOS devices by the TID effects. They demonstrated significant sensitivity to ionizing radiation in both n- and p-channel transistors.[12] Subsequently, Hughes *et al.* discovered that the charges generated within the oxide layer rather than on the oxide surface cause the TID effects.[13] In the following decades, researchers studied the electrical properties of different MOS devices like transistors and capacitors under the irradiation of different sources of ^{60}Co γ-rays, x-rays and high-energy electrons.[14–16] These experiments confirmed that the key mechanism of the TID effects is the accumulation of positive charges in the oxide layer of MOS devices. However, besides the expensive irradiation testing cost,[17] $\Delta V_{\rm th}$ induced by TID is a multiscale dynamic process from e-h pairs generation to accumulation of charged defects. Whereas, in experiments, it is hard to trace the multiscale dynamic behaviors of mobile particles and defects and distinguish their distributions during irradiation.[18] Therefore, it requires an alternative approach based on theoretical simulation/modeling.

The traditional analytical models are commonly used to study TID by solving the rate equations of oxide charged defects ($N_{\rm ot}$) and interface charged defects ($N_{\rm it}$).[19] It is much simple by only considering the two dominant processes including the capture of irradiation-induced holes by oxygen vacancies and the reactions of interface defects with hydrogen molecules (H_2). The model fails to take into account the com-

†These authors contributed equally to this work.
‡Corresponding author. E-mail: ygli@theory.issp.ac.cn

© 2023 Chinese Physical Society and IOP Publishing Ltd

plete interactions, the influence of different irradiation conditions, and the detailed distributions of defects/electric field. In the past decades, the dynamic modeling of the TID effects has also been developed from the original one-dimensional (1D) theoretical model of the oxide layer to the commercial three-dimensional (3D) simulation software of devices.[20,21] In addition, the influences of the H_2 concentration and dose rate on the TID effects were studied in different semiconductor devices.[22,23] In 1988, Srour *et al.* developed a physical model to study the TID process, and attributed it to four steps, that is, e-h pair generation, free carrier transport, bulk charged defect buildup, and interface charged defect formation.[24] Recently, based on Srour's model, Esqueda established a 1D analytical model for the SiO_2 layer to further describe the damage process quantitatively, which is validated by experiments.[25] He provided a comprehensive study of the physical mechanisms contributing to the buildup of bulk and interface charged defects in advanced CMOS technologies. Only two species of defects are considered in his model due to an insufficient understanding of the composition of the oxide layer. More defect species with various configurations and reactions among them need to be clarified and taken into account.[26] Rowsey *et al.* proposed a 1D quantitative model to accurately describe the dynamic behaviors of defects in the oxide layer, with more realistic defect reactions and parameters,[27] especially for H_2 and hydrogenated defects acquired by the first-principles calculations.[28] This research provided new insights into the enhanced low-dose-rate sensitivity (ELDRS) in the isolation oxides prevalent in many bipolar devices. Till now, $\Delta V_{\rm th}$ of MOS devices after irradiation is mainly attributed to the accumulation of oxide charged defects in the oxide layer, through the mechanisms of holes capture or electrons releasing caused by TID-induced e-h pairs generation. However, there are still challenges in fully understanding the mechanism of TID-induced $\Delta V_{\rm th}$. Especially, it is needed to more strictly clarify which defect affects the threshold voltage most and through which mechanism. It is also necessary to quantitatively analyze the influence of different sample/service conditions on the TID effects, and figure out the key factors for the design of high radiation-hardened devices.

In this paper, we adopted new reaction mechanisms and parameters mainly from Rowsey's model,[27] and developed a dynamic model to accurately describe the evolution and distribution of mobile particles and defects in MOS devices by the TID effects. The effects of oxygen vacancy defects and interfacial electric field on the threshold voltage were thus analyzed systematically. This work provides a theoretical guidance for the radiation-hardening-by-design (RHBD) techniques of semiconductor devices.

2. Theoretical model

A 1D dynamic model of mobile particles and defects in the oxide (SiO_2) layer is developed to systematically study the TID effects of MOS devices under γ-ray irradiation. The schematic diagram of the 1D SiO_2 layer of typical MOS devices is shown in Fig. 1. The model can be summarized as follows. First, the initial distributions of defects can be determined by electron paramagnetic resonance measurements.[29] The reaction events and rate coefficients between mobile particles and defects are given by the density functional theory (DFT) calculations.[28] Then, with this information, the continuity equations of mobile particles and defects can be described based on the rate theory. Finally, the finite difference method and the sub-cycle algorithm are employed to solve the stiff ordinary differential equations (ODEs) efficiently. The evolution and distribution of mobile particles and charged defects can thus be obtained by this model. The whole dynamic model framework is shown in Fig. 2.

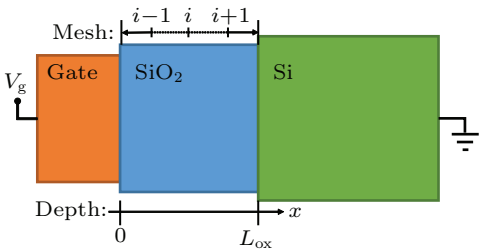


Fig. 1. Schematic diagram of the 1D SiO_2 layer of typical MOS devices with the boundary conditions of the metal gate and Si substrate on the left and right sides, respectively.

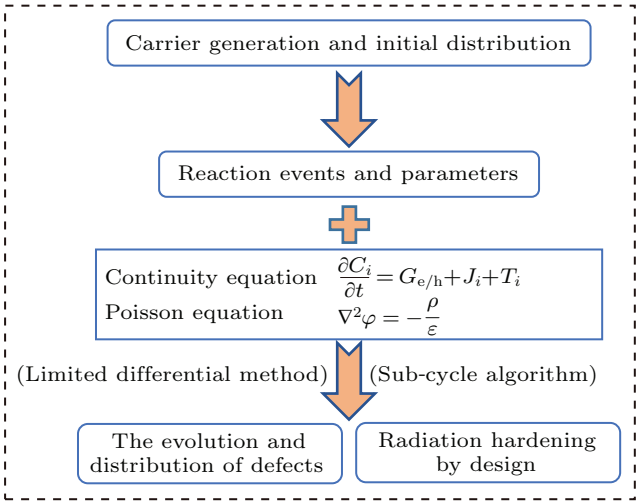


Fig. 2. Dynamical model framework for particles and defects.

2.1. Continuity equations

The dynamic model of mobile particles and defects is based on numerically solving a set of coupled continuity equations, as given by

$$\frac{\partial C_i}{\partial t} = G_i + J_i + T_i. \tag{1}$$

Here C_i represents the concentration of particle i at a certain position at a certain time. G_i, T_i and J_i represent the generation (only for electron/hole), reaction (with other defects) and drift-diffusion (only for mobile particles) rates of particle i, respectively.

According to experimental findings, the following reasonable approximations are applied here:

1) 18 types of mobile particles and fixed defects are involved. Mobile particles include electrons (e), holes (h), hydrogen molecules (H_2) and protons (H^+). Fixed defects are divided into bulk and interface defects. Bulk defects include shallow ($V_{o\delta}$, $V_{o\delta}H$, $V_{o\delta}H_2$, $V_{o\delta}^+$, $V_{o\delta}H^+$, $V_{o\delta}H_2^+$) and deep ($V_{o\gamma}$, $V_{o\gamma}H$, $V_{o\gamma}H_2$, $V_{o\gamma}^+$, $V_{o\gamma}H^+$, $V_{o\gamma}H_2^+$) energy level defects. The interface defects are silicon–hydrogen bonds (Si–H) and dangling bonds (Si–).[29] The dominating 18 particles and defects are included in the model to increase the efficiency. This approximation is reasonable enough for all known damage-related defects were considered and the results obtained could be quantitatively compared with the experimental results.

2) Before irradiation, the initial defect concentration in the oxide layer seriously depends on the fabricating process of MOS devices, which is uniform distribution approximately. The concentration values[29,30] under typical conditions used in the simulation are given in Table 1.

3) Only the de-passivated reaction ($H^+ + \text{Si–H} \rightarrow N_{it} + H_2$) with the thermal activation energy of 0.2 eV is involved, while the passivated reaction with the energy of 1.3 eV cannot occur at the temperature studied here.[31]

4) Since the mobility of charged defects is much lower than that of carriers under electric field, they are reasonably treated as immobile. In addition, the reactions of electron capture and emission by charged defects occur locally. Therefore, the migration of the charged defect has nearly no effect on the simulation results.

2.1.1. Generation of electron–hole pairs

As γ-rays pass through the oxide layer, high-energy photons transfer energy to electrons to excite uniform e-h pairs through direct or indirect ionizing processes. The generation rate of e-h pairs induced by the ionizing irradiation is given as follows:[32]

$$G_{e/h} = Y \cdot G_0 \cdot R, \tag{2}$$

where G_0 represents the density of e-h pairs per unit ionizing dose, Y is the survival rate of the e-h pairs after the initial recombination, which is set to be 0.01 for SiO_2 under γ-ray irradiation,[18] and R is the dose rate (rad/s).

2.1.2. Reactions of mobile particles with defects

The commonly oxidation process will produce 10^{14}–10^{18} cm^{-3} oxygen vacancy ($V_{o\gamma}$ and $V_{o\delta}$) and hydrogenated oxygen vacancy ($V_{o\delta}H$, $V_{o\delta}H_2$, $V_{o\gamma}H$ and $V_{o\gamma}H_2$) defects in the oxide layer,[33] whose concentrations are given in Table 1. H_2 is also introduced during the oxidation process, typically with a concentration of 10^{14}–10^{20} cm^{-3}.[26] Oxygen vacancy can trap a hole to generate a positively charged defect that can crack H_2 to release a H^+ or serve as a recombination center. Hydrogenated oxygen vacancy also can trap a hole to generate a positively charged defect that can directly release a H^+/H_2 or serve as a recombination center.[25,29,30] The rate coefficients α and β are formulated based on the reaction barriers obtained by DFT. The specific reaction events and rate coefficients are listed in Table 1. The reaction rates of mobile particles with defects are determined by the rate theory, which is proportional to the reactant concentrations. Comprehensively considering all reaction events (Table 1), the net generation rate of particle i is given by[29]

$$T_i = -\sum_j \alpha C_i C_j + \sum_{m+n\rightarrow i} \beta C_m C_n, \tag{3}$$

where j, m and n are termed as the other reactants, and α and β represent the forward and reverse reaction rate coefficients, respectively.

An important parameter is the density of N_{ot}, in units of [cm^{-2}], which can be determined by integrating the distribution of each oxide charged defect as[25]

$$C_{Not} = \int_0^{L_{ox}} \frac{x}{L_{ox}} \left(C_{V_{o\delta}^+} + C_{V_{o\delta}H^+} + C_{V_{o\delta}H_2^+} + C_{V_{o\gamma}^+} + C_{V_{o\gamma}H^+} + C_{V_{o\gamma}H_2^+}\right) \mathrm{d}x, \tag{4}$$

where L_{ox} is the thickness of the oxide layer, and x refers to the distance from the gate.

In the high-temperature environment of hundreds of degrees Celsius during the oxidation process, the silicon dangling bonds at the Si/SiO_2 interface are passivated to form Si–H bonds. During ionizing irradiation, the generated H^+ will react with Si–H bonds to form H_2 and the interface charged defect Si– (N_{it}),[31] that is, $H^+ + \text{Si–H} \rightarrow N_{it} + H_2$. The corresponding rate equation of N_{it} formation can be given by[18]

$$\frac{\partial C_{N_{it}}}{\partial t} = \sigma_{Si-H,H^+} \left(C_{Si-H} - C_{N_{it}}\right) J_{H^+}, \tag{5}$$

where, σ_{Si-H,H^+} is the capture cross-section, C_{Si-H} and $C_{N_{it}}$ are the surface densities of the interfacial Si–H bonds and charged Si– bonds, respectively.

Table 1. Reaction events and rate coefficients.

Defect	Concentration (cm^{-3})	Chemical reaction	α (cm^3/s)	β
$V_{o\gamma}$	10^{15}	$V_{o\gamma}+h^+ \leftrightarrow V_{o\gamma}^+$	1.03×10^{-13}	1.26×10^{-62} s^{-1}
		$V_{o\gamma}^+ + e^- \leftrightarrow V_{o\gamma}$	1.97×10^{-14}	3.21×10^{-138} s^{-1}
		$V_{o\gamma}^+ + H_2 \leftrightarrow V_{o\gamma}H_2^+$	4.02×10^{-21}	1.90×10^{5} s^{-1}
		$V_{o\gamma}+H^+ \leftrightarrow V_{o\gamma}H^+$	8.21×10^{-37}	5.04×10^{-22} s^{-1}
$V_{o\gamma}H$	10^{14}	$V_{o\gamma}H+h^+ \leftrightarrow V_{o\gamma}H^+$	1.03×10^{-13}	1.26×10^{-62} s^{-1}
		$V_{o\gamma}H^+ + e^- \leftrightarrow V_{o\gamma}H$	2.06×10^{-7}	5.07×10^{-113} s^{-1}
		$V_{o\gamma}^+ + H_2 \leftrightarrow V_{o\gamma}H+H^+$	1.92×10^{-19}	1.03×10^{-19} cm^3/s
		$V_{o\gamma}H+H^+ \leftrightarrow V_{o\gamma}H_2^+$	1.03×10^{-19}	3.81×10^{5} s^{-1}
$V_{o\gamma}H_2$	10^{15}	$V_{o\gamma}H_2+h^+ \leftrightarrow V_{o\gamma}H_2^+$	1.03×10^{-13}	4.16×10^{3} s^{-1}
		$V_{o\gamma}H_2^+ + e^- \leftrightarrow V_{o\gamma}H_2$	2.06×10^{-7}	3.21×10^{-138} s^{-1}
$V_{o\delta}$	10^{18}	$V_{o\delta}+h^+ \leftrightarrow V_{o\delta}^+$	1.03×10^{-13}	4.16×10^{3} s^{-1}
		$V_{o\delta}^+ + e^- \leftrightarrow V_{o\delta}$	2.06×10^{-7}	3.21×10^{-113} s^{-1}
		$V_{o\delta}^+ + H_2 \leftrightarrow V_{o\delta}H_2^+$	3.35×10^{-31}	3.98×10^{3} s^{-1}
		$V_{o\delta}+H^+ \leftrightarrow V_{o\delta}H^+$	1.03×10^{-19}	3.81×10^{5} s^{-1}
$V_{o\delta}H$	10^{14}	$V_{o\delta}H+h^+ \leftrightarrow V_{o\delta}H^+$	1.03×10^{-13}	4.16×10^{3} s^{-1}
		$V_{o\delta}H^+ + e^- \leftrightarrow V_{o\delta}H$	2.06×10^{-7}	2.00×10^{-37} s^{-1}
		$V_{o\delta}^+ + H_2 \leftrightarrow V_{o\delta}H+H^+$	1.46×10^{-34}	1.03×10^{-19} cm^3/s
		$V_{o\delta}H+H^+ \leftrightarrow V_{o\delta}H_2^+$	1.03×10^{-19}	3.81×10^{5} s^{-1}
$V_{o\delta}H_2$	10^{15}	$V_{o\delta}H_2+h^+ \leftrightarrow V_{o\delta}H_2^+$	1.03×10^{-13}	4.16×10^{3} s^{-1}
		$V_{o\delta}H_2^+ + e^- \leftrightarrow V_{o\delta}H_2$	2.06×10^{-7}	3.21×10^{-138} s^{-1}
Si–H	10^{13}	Si–H+$H^+ \leftrightarrow N_{it}+H_2$	–	–

2.1.3. Drift-diffusion of mobile particles

Mobile particles can diffuse driven by the gradient of concentration, and mobile charged particles can drift under the electric field in the SiO_2 layer. The drift-diffusion equation is given as follows:[34]

$$J_i = D_i\frac{\partial^2 C_i}{\partial x^2} - \mu_i\left(E\frac{\partial C_i}{\partial x} + C_i\frac{\partial E}{\partial x}\right), \tag{6}$$

where μ_i represents the mobility of mobile charged particles, D_i=$\mu_i k_B T/q$ represents the diffusion coefficients of mobile particles, and E represents the electric field along the grid direction.

The mobility of electrons in SiO_2 is much higher than that of holes, so electrons quickly flow out of the oxide layer, while holes react with the oxide defects ($V_{o\delta}$, $V_{o\delta}H$, $V_{o\delta}H_2$, $V_{o\gamma}$, $V_{o\gamma}H$ and $V_{o\gamma}H_2$) in the oxide layer to produce oxide charged defects ($V_{o\delta}^+$, $V_{o\delta}H^+$, $V_{o\delta}H_2^+$, $V_{o\gamma}^+$, $V_{o\gamma}H^+$ and $V_{o\gamma}H_2^+$).[26] The accumulation of the oxide charged defects results in the formation of a built-in electric field in the oxide layer. The electric field can be obtained by solving the Poisson equation[26]

$$\nabla\cdot E_{ot} = \frac{\rho}{\varepsilon_{ox}\varepsilon_0}, \tag{7}$$

where

$$\begin{aligned}\rho \;=\; & e_c\big(C_h + C_{H^+} + C_{V_{o\delta}^+} + C_{V_{o\delta}H^+} + C_{V_{o\delta}H_2^+} \\ & + C_{V_{o\gamma}^+} + C_{V_{o\gamma}H^+} + C_{V_{o\gamma}H_2^+} - C_e\big).\end{aligned} \tag{8}$$

Here, ρ is the total charge density in the oxide layer, e_c is the elementary charge, $\varepsilon_{ox}$is the relative permittivity of SiO_2, and ε_0 is the vacuum permittivity.

In addition, the constant electric field induced by the accumulation of interface charged defects in the oxide layer can be given by taking the gate–SiO_2–Si system as a parallel plate capacitor as[35,36]

$$E_{it} = \frac{\rho_{it}}{\varepsilon_{ox}\varepsilon_0}, \tag{9}$$

where $\rho_{it} = eC_{N_{it}}$ represents the charge density at the interface.

2.2. Numerical method

The finite difference method with a uniform spatial grid is adopted for solving the partial differential equations (PDEs). Here the *lsoda* solver of the *C* version is employed to solve the corresponding ODEs.

2.2.1. Boundary conditions.

As shown in Fig. 1, the boundary conditions of the oxide layer in solving the ODEs are set as follows:

1) For the mobile particles except for protons, the absorption boundary conditions are adopted at the interfaces of both gate/SiO_2 and Si/SiO_2 as

$$C_i = 0. \tag{10}$$

2) For protons, the absorption boundary conditions are also adopted at the interface of gate/SiO_2 as

$$C_{H^+} = 0, \tag{11}$$

and the third boundary condition on the interface of Si/SiO_2 is typically set as

$$J_{H^+}\cdot\boldsymbol{n} = kC_{H^+}, \tag{12}$$

to consider the reaction with the interface defects, where $k = 10^{-11}$ is the reaction coefficient of H^+ and Si–H.

2.2.2. Sub-cycle algorithm

The continuity equation includes the evolution of both mobile particles and defects, with the former rates generally much higher than the latter. It makes the above ODEs become typical stiff equations, leading to very low solution efficiency. Thus, we introduced a sub-cycle algorithm[37] to accelerate the solution of these ODEs. The basic idea of the sub-cycle algorithm is to select different time steps at different time scales of particles and defects in solving ODEs. Time nodes are divided into two groups. One is the main cycle group T_i corresponding to defect dynamics, which represents the global time step. The other is the sub-cycle group t_i corresponding to particle dynamics, which represents the local time step that is much smaller than the global time step.

In the numerical solution, the time nodes are circularly advanced. First, the continuity equation of mobile particles is solved and the local time nodes, t_1, t_2, t_3, ..., are iterated successively, until the global time node T_1 is reached. Secondly, the continuity equation of defects is iterated to the global time node T_1 to complete the iteration. Then, the same iterations are repeated until the final time node is reached.

3. Results

In this section, we firstly verified our model according to the experimental data of an NPN-type MOS capacitor irradiated by γ-rays.[25] Secondly, we gave the evolution and distribution of defects and electric field in the SiO_2 layer to study the TID-induced threshold voltage shifts. Finally, we studied several hardened methods for the threshold voltage shifts. The physical parameters involved in the model are given in Table 2.

Table 2. Physical parameters used in simulations.

Physical parameters	Value	Refs.
Oxide layer thickness (L_{ox})	200 nm	[24]
Oxide layer relative permittivity (ε_{ox})	3.9	[24]
Generation rate of e-h pairs (G_0)	8.1×10^{12} cm^{-3}·rad^{-1}	[24]
Electron mobility (μ_e)	20 V·cm^2·s^{-1}	[24]
Hole mobility (μ_h)	10^{-6} V·cm^2·s^{-1}	[24]
Proton mobility (μ_{H^+})	4×10^{-9} V·cm^2·s^{-1}	[28]
Hydrogen diffusion coefficient (D_{H_2})	10^{-9} cm^2·s^{-1}	[28]
Capture cross section of Si–H bond for proton (σ_{Si-H,H^+})	10^{-11} cm^2	[24]
Reaction coefficient of Si–H bond with proton (k)	10^{-11} cm^2·s^{-1}	[28]

3.1. Validation and verification

The simulated densities of oxide (N_{ot}) and interface (N_{it}) charged defects are compared with the experimental ones[25] to verify our model. Figure 3 shows the time evolution of the densities of N_{ot} and N_{it}, under the time of 1.5×10^4 s with the dose rate of 20 rad/s at 300 K. The capacitance–gate voltage curves of the irradiated devices under three different TIDs were measured to determine the average densities of N_{ot} and N_{it}. Typically, both N_{ot} and N_{it} increase gradually with irradiation time and tend to saturation. The simulation results are almost consistent with the experimental ones.

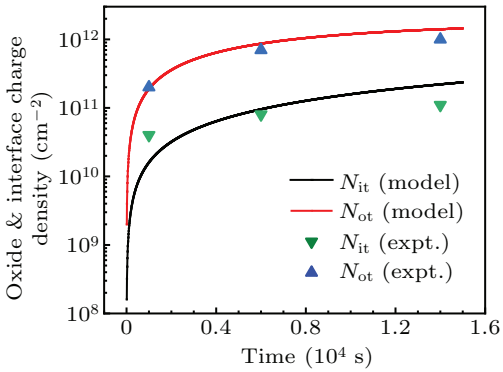


Fig. 3. Comparison of the evolution of N_{ot} and N_{it} with the experiment for the MOS capacitor with a 200 nm SiO_2 layer under 5 V bias.

In addition, N_{ot} is higher than N_{it}, which is mainly determined by the initial densities of oxygen vacancies and Si–H bonds. Thus, our model should be reasonable enough for simulating the TID effects.

3.2. Distribution and evolution of charged particles and electric field

Compared to N_{it}, N_{ot} plays a dominant role in TID-induced ΔV_{th}.[35] Therefore, it is necessary to study the key factors of the oxide charged defects for the TID effects, such as the composition, distribution and evolution. Here the distributions of oxide charged defects, carriers, charge and electric field are simulated under the TID of 10 krad with the dose rate of 10 rad/s at 300 K. The distribution of carriers induced by irradiation determines the distributions of oxide charged defects. The carriers and charged defects will cause the formation of the built-in electric field that changes the distribution of the total electric field, which will in turn affect the distribution of carriers and charged defects.

Figure 4(a) shows the distributions of different oxide charged defects. Although the initial density of $V_{o\delta}$ is the highest in the oxide layer, $V_{o\gamma}^+$ and $V_{o\gamma}H^+$ are the main components of the oxide charged defects. It is because the capture probability (1.97×10^{-14}) of $V_{o\gamma}^+$ for electrons ($V_{o\gamma}^+ + e \rightarrow$

$V_{o\gamma}$) is comparable to that (1.03×10^{-13}) of $V_{o\gamma}$ for holes ($V_{o\gamma} + h \rightarrow V_{o\gamma}^{+}$) and lower than the electron capture probability (2.06×10^{-7}) of other charged defects ($V_{o\delta}^{+} + e \rightarrow V_{o\delta}$). Thus, it is easier for $V_{o\gamma}$ to form $V_{o\gamma}^{+}$ than $V_{o\delta}$ to form $V_{o\delta}^{+}$. Also shown in Fig. 4(a), with the increasing distance from the gate, the densities of charged oxygen vacancies ($V_{o\gamma}^{+}$ and $V_{o\delta}^{+}$) and charged singly-hydrogenated oxygen vacancies ($V_{o\gamma}H^{+}$ and $V_{o\delta}H^{+}$) slowly increase in the oxide layer but decrease at the boundary. It is mainly because the changes in their densities are determined by the distribution of hole density through capturing holes that are low at the boundaries, as shown in Fig. 4(b). With the positive electric field, the density of holes and electrons becomes higher and lower as the distance from the gate increases, respectively. But because they flow out at the boundaries, the densities of holes and electrons decrease rapidly at the Si/SiO_2 and gate/SiO_2 interfaces, respectively. Due to the competition between the electric field drive and the boundary absorption, the positions with the highest hole and electron densities are about 30 nm from the Si/SiO_2 and gate/SiO_2 boundaries, respectively. Therefore, the accumulation distribution of holes determines the distributions of $V_{o\gamma}^{+}$, $V_{o\gamma}H^{+}$, $V_{o\delta}^{+}$ and $V_{o\delta}H^{+}$, also with the peak at 30 nm from the Si/SiO_2 interface. Although the proportion of charged doubly-hydrogenated vacancies ($V_{o\gamma}H_2^{+}$ and $V_{o\delta}H_2^{+}$) is not high, they promote the formation of major charged defects ($V_{o\gamma}^{+}$ and $V_{o\gamma}H^{+}$). With the increasing distance from the gate, their densities first increase and then decrease, and rise again at the Si/SiO_2 boundary. From 0 to 30 nm, the reaction of the initial defects capturing holes is dominant, and their densities are affected by the holes. From 30 nm to 200 nm, the releasing proton reaction of the charged defects is dominant, and their densities are affected by $V_{o\gamma}^{+}$, $V_{o\gamma}H^{+}$, $V_{o\delta}^{+}$ and $V_{o\delta}H^{+}$. The spatial distributions of charged defects and carriers contribute to the spatial charge distribution, as shown in Fig. 4(c). The trend of its distribution is determined by all the free charges mainly contributed by $V_{o\gamma}^{+}$ and $V_{o\gamma}H^{+}$. The charge density near the Si/SiO_2 interface is higher than that in the oxide layer, and the peak is also located at 30 nm from the Si/SiO_2 interface. The spatial charges further induce the built-in electric field, as shown in Fig. 4(d). The initial electric field is uniform, while the total and build-in electric fields increase with the position after irradiation. The built-in electric field is negative and positive near the gate/SiO_2 and Si/SiO_2 interfaces, respectively. The reversal point locates at 120 nm, which means that the electric field created by the spatial charges is negative in the 0–120 nm range and positive in the range of 120–200 nm. This is related to the position of the peak of the spatial charges. $V_{o\gamma}^{+}$ dominates the distribution of the space charges, then the spatial charges determine the distribution of the built-in electric field. And the electric field at the Si/SiO_2 interface ultimately affects the change of the threshold voltage. The positive built-in electric field at the Si/SiO_2 interface has an enhancement effect on the initial electric field, as shown in Fig. 4(d). It will increase the carrier (electron) density in the channel, and the required conduction voltage (that is, the device threshold voltage) is reduced accordingly.

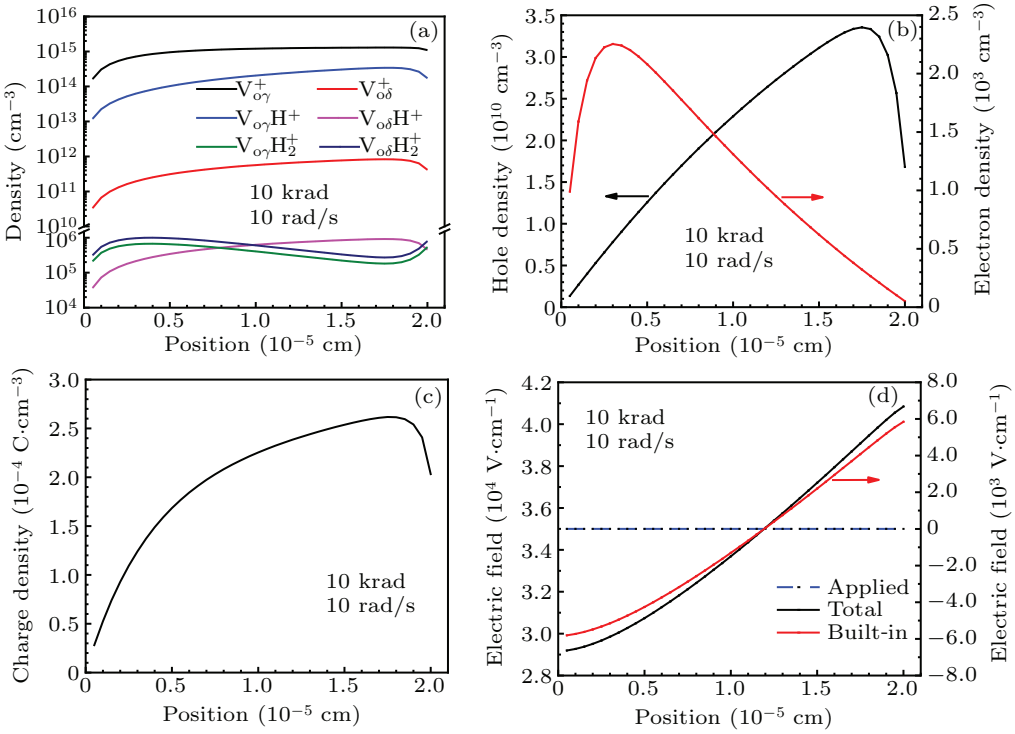


Fig. 4. Distributions of (a) different oxide charged defects, (b) carriers, (c) total charge density and (d) electric fields, under the TID of 10 krad with the dose rate of 10 rad/s at 300 K.

As mentioned above, $V_{o\gamma}^{+}$ and $V_{o\gamma}H^{+}$ are the main oxide charged defects. $V_{o\gamma}^{+}$ is produced by three main reaction channels, that is, $V_{o\gamma} \rightarrow V_{o\gamma}^{+}$ (channel 1), $V_{o\gamma}H \rightarrow V_{o\gamma}^{+}$ (channel 2) and $V_{o\gamma}H_2 \rightarrow V_{o\gamma}^{+}$ (channel 3). $V_{o\gamma}H^{+}$ is also formed by three reaction channels of $V_{o\gamma}H \rightarrow V_{o\gamma}H^{+}$ (channel 4), $V_{o\gamma} \rightarrow V_{o\gamma}H^{+}$ (channel 5) and $V_{o\gamma}H_2 \rightarrow V_{o\gamma}H^{+}$ (channel 6). We simulated the evolution of the densities of $V_{o\gamma}^{+}$ and $V_{o\gamma}H^{+}$ under the TID of 10 krad with the dose rate of 10 rad/s at room temperature. Figure 5(a) shows the densities of $V_{o\gamma}^{+}$ as a function of TID. $V_{o\gamma}^{+}$ increases with increasing TID and finally tends to saturation that exceeds the initial value of $V_{o\gamma}$ (blue line). The total density of $V_{o\gamma}^{+}$ and $V_{o\gamma}$ (red line) is higher than the initial value of $V_{o\gamma}$, because of other contributions (purple line) from channels 2 and 3 in addition to channel 1. The contribution of channel 1 dominates the generation of $V_{o\gamma}^{+}$ with one order of magnitude higher than the others. A similar trend can be found for $V_{o\gamma}H^{+}$, as shown in Fig. 5(b). $V_{o\gamma}H^{+}$ increases with increasing TID and finally tends to saturation that exceeds the initial value of $V_{o\gamma}H$ (blue line). The total density of $V_{o\gamma}H^{+}$ and $V_{o\gamma}H$ (red line) is higher than the initial value of $V_{o\gamma}H$, this is because of other contributions (purple line) from channels 5 and 6 in addition to channel 4. This result proves that $V_{o\gamma}H_2^{+}$ and $V_{o\delta}H_2^{+}$ are much important for the TID effects.

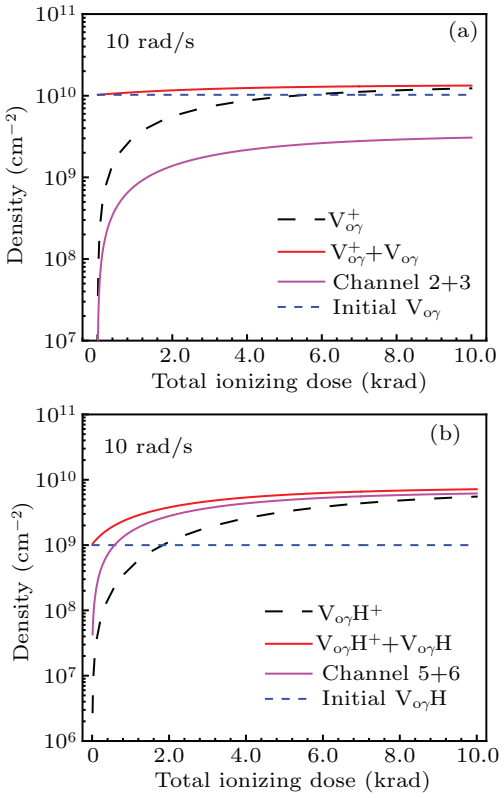


Fig. 5. Density of (a) $V_{o\gamma}^{+}$ and (b) $V_{o\gamma}H^{+}$ in the oxide layer as a function of TID at the dose rate of 10 rad/s at 300 K.

In addition, the rise rates of the densities of $V_{o\gamma}^{+}$ and $V_{o\gamma}H^{+}$ slow down with increasing TID, because the electric field inhibits the transport of holes and thus their formation rate. Figure 6(a) shows the spatial distributions of the electric fields under different TIDs. The electric fields near the gate/SiO_2 interface decrease with increasing TID, which slows down the transport of holes away from the gate. The electric fields near the Si/SiO_2 interface increase with increasing TID, which accelerates hole outflow from the oxide layer. The decrease in the density of holes in the oxide layer leads to a decrease in the probability of holes being captured to form charged defects. Therefore, with increasing TID, the growth rate of densities of $V_{o\gamma}^{+}$ and $V_{o\gamma}H^{+}$ slows down. When the generation and consumption rates balance, their density tends to saturation. The ionization damage induced by the TID will reach saturation, which means that the TID effect has the maximum limit, and there are devices that can withstand the maximum damage. To further explore the influence of TID on the electric field at the interface, Fig. 6(b) shows the relationship between the electric field at the Si/SiO_2 interface with TID. The electric field at the Si/SiO_2 interface (E_{Si/SiO_2}) increases with increasing TID (D), satisfying the universal 2/3 power law as $E_{Si/SiO_2} \propto D^{2/3}$. The model is thus verified again by the 2/3 power law of the experiment.[38] As the TID increases, the threshold voltage decreases. It can also be seen from the figure that with increasing TID, the difference between E_{Si/SiO_2} before and after irradiation is also increasing, which is as high as 17% of the initial electric field at 10 krad. For a typical grid in MOS devices, the electric field at the Si/SiO_2 interface can be simply described as follows:

$$E_{Si/SiO_2} = E_{applied} + E_{built-in} = V_g/L_{ox} + \rho_{tot}/\varepsilon_0\varepsilon_{ox}, \quad (13)$$

where V_g is the gate voltage, L_{ox} is the thickness of the oxide layer, $\rho_{tot} \approx kD^{2/3}$[38] is the density of space charge, and ε_{ox} is the relative permittivity of the oxide layer. The difference in the electric field is up to 17% after irradiation due to the contribution of space charges (mainly $V_{o\gamma}^{+}$ and $V_{o\gamma}H^{+}$). It means that the larger TID is, the larger ΔV_{th} induced by TID would be.

The whole process of threshold voltage shifts induced by TID is shown in Fig. 7. The TID effect induces the generation of e-h pairs at first. In the case of positive gate voltage, the holes and electrons move towards the Si/SiO_2 and gate/SiO_2 interfaces, respectively. For the mobility of holes in SiO_2 is much slower than that of electrons, under the action of the electric field, the holes remain in the oxide layer. Meanwhile, most holes are captured by $V_{o\gamma}$ to form $V_{o\gamma}^{+}$ during movement, and $V_{o\gamma}^{+}$ are mainly accumulated near the Si/SiO_2 interface. The above processes will induce the built-in electric field, which enhances the total electric field at the Si/SiO_2 interface that satisfies the universal 2/3 power law with TID, and causes the increase of carrier density in the channel, resulting in the reduction of the threshold voltage of the MOS devices finally.

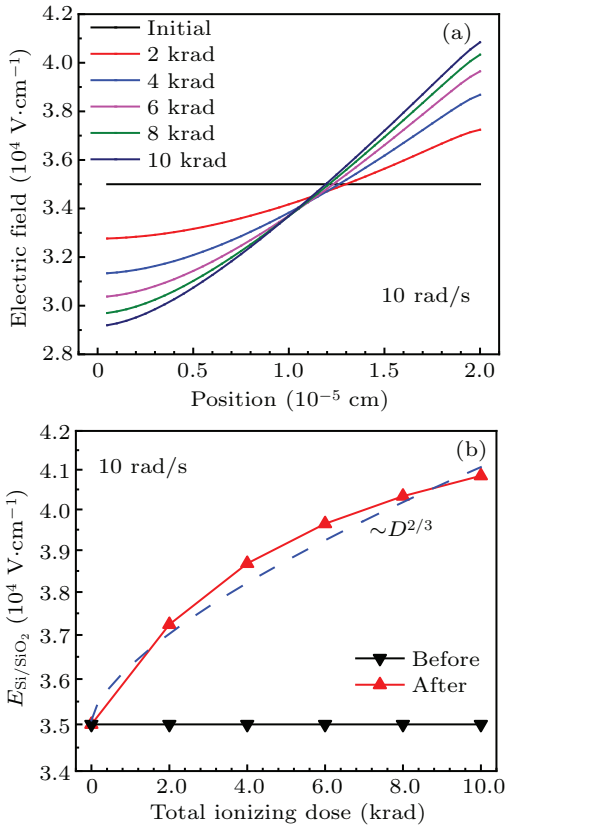


Fig. 6. (a) Spatial distributions of the electric fields in the oxide layer under different TIDs. (b) Electric fields at the Si/SiO_2 interface as a function of TID at the dose rate of 10 rad/s at 300 K.

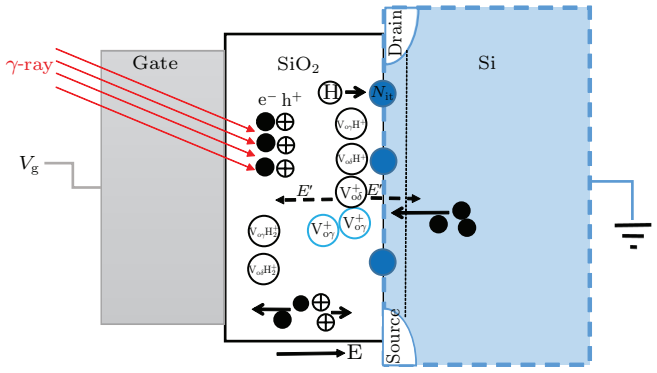


Fig. 7. Schematic diagram of the threshold voltage reduction induced by TID.

3.3. Hardened methods for the threshold voltage shifts

From the analysis of Subsection 3.2, it can be seen that the electric field at the Si/SiO_2 interface plays a major role on ΔV_{th} induced by TID. Therefore, it is necessary to control the interfacial electric fields under different conditions to design high radiation-hardened devices. As shown in Eq. (13), in addition to the space charges mentioned above, there are the thickness (L_{ox}) and the relative permittivity of the oxide layer (ε_{ox}), the gate voltage (V_g), all of which are adjustable factors. In the following, we will investigate the influence of the above three factors (L_{ox}, $\varepsilon_{ox}$and V_g) on the electric field at the Si/SiO_2 interface, under the TID of 10 krad with the dose rate of 10 rad/s at 300 K.

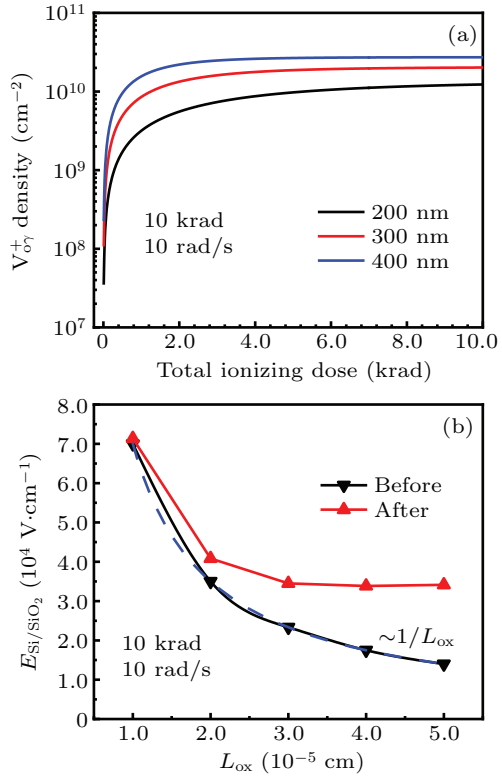


Fig. 8. (a) Density of $V_{o\gamma}^+$ as a function of TID under the different thicknesses of the oxide layer. (b) Electric fields at the Si/SiO_2 interface before and after irradiation as a function of the thickness of the oxide layer.

First, we simulated the influence of L_{ox} on $V_{o\gamma}^+$ and E_{Si/SiO_2}. Figure 8(a) shows the change of the densities of $V_{o\gamma}^+$ with TID under different L_{ox}. Under the same TID, the thinner the oxide layer, the lower the density of $V_{o\gamma}^+$ in the oxide layer. Because the thinner the oxide layer is, the more easily the holes in the oxide layer flow out, which reduces the density of holes and their capture probability by $V_{o\gamma}$ to form $V_{o\gamma}^+$. In addition, as L_{ox} increases, it is faster for $V_{o\gamma}^+$ to tend to saturation, which also indicates that the thick oxide layer increases the capture probability of holes by $V_{o\gamma}$, and thus increases the generation rate of $V_{o\gamma}^+$ which will reach saturation faster. The change in density of $V_{o\gamma}^+$ will affect the electric field at the Si/SiO_2 interface. Figure 8(b) shows the electric fields at the Si/SiO_2 interface before and after γ-ray irradiation as a function of L_{ox}. After irradiation, with increasing L_{ox}, E_{Si/SiO_2}decreases and the decreasing rate slows down rapidly. There is an obvious inflection point at 200 nm. Less than 200 nm, E_{Si/SiO_2} is mainly contributed by $E_{applied}$, and the relationship of E_{Si/SiO_2} with L_{ox} follows $E_{Si/SiO_2} \propto 1/L_{ox}$ according to Eq. (13). Over 200 nm, E_{Si/SiO_2} is affected by both the increase of $E_{built-in}$ and the decrease of $E_{applied}$. E_{Si/SiO_2} no longer satisfies the relationship of $1/L_{ox}$ and is mainly controlled by $E_{built-in}$. In addition, with increasing L_{ox}, the difference between E_{Si/SiO_2} before and after irradiation also increases, which means that the thickness of the oxide layer has a great influence on the electric field at the Si/SiO_2 interface after irradiation. Reducing the thickness of the oxide

layer should be much beneficial to inhibit the reduction of the threshold voltage induced by TID.

In view of the influence of the permittivity of the oxide layer on $V_{o\gamma}^{+}$ and E_{Si/SiO_2}, the densities of $V_{o\gamma}^{+}$ with TID at different ε_{ox} are shown in Fig. 9(a). We found that the density of $V_{o\gamma}^{+}$ almost overlaps under different ε_{ox}, which means that changing ε_{ox} has little influence on the density of ε_{ox} after irradiation. However, E_{Si/SiO_2} will decrease rapidly with increasing ε_{ox} as shown in Fig. 9(b). This is because the permittivity changes E_{Si/SiO_2} by changing $E_{built-in}$ but $E_{applied}$. Therefore, the relationship between E_{Si/SiO_2} and ε_{ox} is the same as that of $E_{applied}$, $E_{Si/SiO_2} \propto 1/\varepsilon_{ox}$ according to Eq. (13). With increasing ε_{ox}, the difference between E_{Si/SiO_2} after and before irradiation becomes small. Thus, the permittivity has an obvious influence on E_{Si/SiO_2} during irradiation. Increasing the permittivity could effectively inhibit the reduction of the threshold voltage induced by TID.

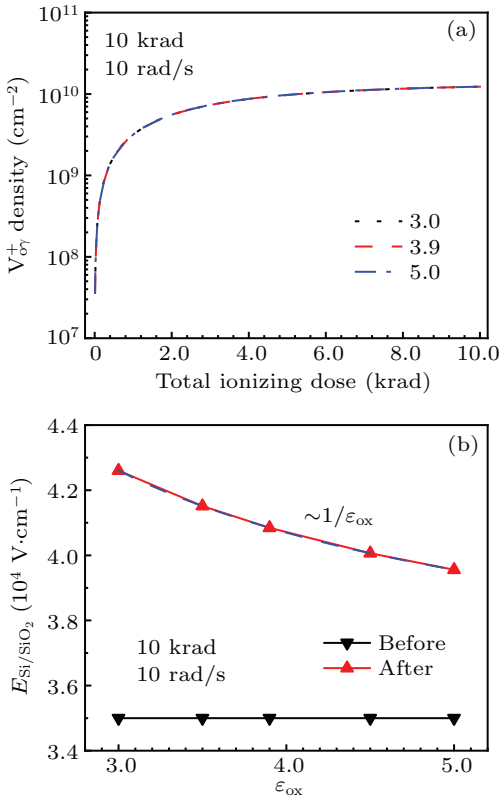


Fig. 9. (a) Density of $V_{o\gamma}^{+}$ with TID at different relative permittivities. (b) Electric fields at the Si/SiO_2 interface before and after irradiation with relative permittivity.

The influence of the gate voltage on $V_{o\gamma}^{+}$ and E_{Si/SiO_2} is also studied. The densities of $V_{o\gamma}^{+}$ with TID at different V_g are shown in Fig. 10(a). The higher V_g is, the lower the density of $V_{o\gamma}^{+}$ is in the oxide layer. It could be because the higher V_g is, the greater $E_{applied}$ is in the oxide layer. The holes are easier to flow out, thus reducing the capture probability of holes by $V_{o\gamma}$ to suppress the generation of $V_{o\gamma}^{+}$. Moreover, with the decrease of V_g, $V_{o\gamma}^{+}$ reaches saturation faster, because the lower V_g increases the probability of holes being captured by $V_{o\gamma}$ to generate $V_{o\gamma}^{+}$. Figure 10(b) shows the change of E_{Si/SiO_2} after and before irradiation and their ratios ($E_{Si/SiO_2}/E_{applied}$) with V_g. The ratio of $E_{Si/SiO_2}/E_{applied}$ increases with decreasing V_g. The ratio can be up to 2.5 when V_g is smaller than 0.4 V, and vanish when V_g is larger than 1.0 V because $E_{built-in}$ can be neglected compared to $E_{applied}$. This means that the TID effect greatly influences E_{Si/SiO_2} when V_g is small. Thus, increasing V_g can effectively inhibit the harmful influence. As shown in Eq. (13), the slope of E_{Si/SiO_2} is related to the thickness of the oxide layer by $1/L_{ox}$, reducing the thickness can effectively reduce the harmful influence by TID.

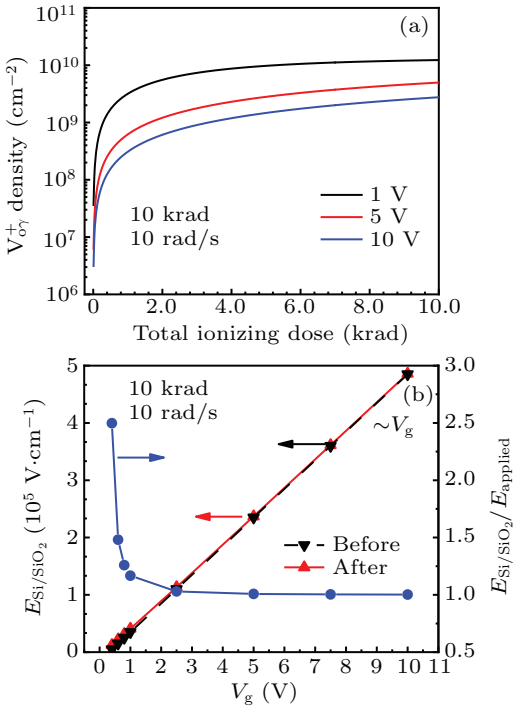


Fig. 10. (a) Density of $V_{o\gamma}^{+}$ with TID at different gate voltages. (b) The interfacial electric field at the Si/SiO_2 interface after and before irradiation and their ratio with the gate voltage.

4. Conclusions

In summary, we have developed a 1D dynamic model of mobile particles and defects in the oxide (SiO_2) layer of a typical NMOS device under γ-ray irradiation, by combining rate equations and Poisson's equation. The model is applied to simulate the distributions and evolution of charged defects and the electric field to reveal the key mechanisms of threshold voltage shifts induced by TID. The main process is the accumulation of $V_{o\gamma}^{+}$ induced by TID near the Si/SiO_2 interface, which enhances the electric field at the interface and increases the carrier density in the channel by the electric field, thereby reducing the threshold voltage. Finally, considering these mechanisms, we pointed out that the oxide layer should be synthesized as thin as possible and with high enough permittivity in the oxidation process of device manufacturing. And the TID effects can be weakened by selecting devices with a higher threshold voltage.

Acknowledgements

Project supported by the Science Challenge Project of China (Grant No. TZ2018004), the National Natural Science Foundation of China (Grant Nos. 11975018 and 11775254), the National MCF Energy R&D Program of China (Grant No. 2018YEF0308100), and the outstanding member of Youth Innovation Promotion Association CAS (Grant No. Y202087).

References

[1] Benton E R and Benton E V 2001 *Nucl. Instr. Meth. B* **184** 255
[2] Sajid M, Chechenin N G, Sill Torres F, Nabeel Hanif M, Gulzari U A, Arslan S and Khan E U 2018 *Nucl. Instr. Meth. B* **428** 30
[3] Foster C C 2003 *MRS Bull.* **28** 136
[4] Schwank J R, Shaneyfelt M R, Fleetwood D M, Felix J A, Dodd P E, Paillet P and Ferlet-Cavrois V 2008 *IEEE Trans. Nucl. Sci.* **55** 1833
[5] Dodd P E 2005 *IEEE Trans. Device Mater. Rel.* **5** 343
[6] Adell P C and Scheick L Z 2013 *IEEE Trans. Nucl. Sci.* **60** 1929
[7] Hughes H L and Benedetto J M 2003 *IEEE Trans. Nucl. Sci.* **50** 500
[8] Choi Y, Ha D, King T and Hu C 2001 *IEEE DRC* 85–86
[9] Chen Y, Xu D, Xu K, Zhang N, Liu S, Zhao J, Luo Q, Snyman L W and Swart J W 2019 *Chin. Phys. B* **28** 107801
[10] Oldham T R and McLean F B 2003 *IEEE Trans. Nucl. Sci.* **50** 483
[11] Ma T C and Dressendorfer P V **1989** *Ionizing Radiation Effects in MOS Devices and Circuits* (New York: Wiley)
[12] Hughes H L and Giroux R R 1964 *Electronics* **37** 58
[13] Hughes H L 1965 *IEEE Trans. Nucl. Sci.* **12** 53
[14] Kooi E 1965 *Philips Res. Rept.* **20** 306
[15] Zaininger K H 1966 *Appl. Phys. Lett.* **8** 140
[16] Szedon J R and Sandor J E 1965 *Appl. Phys. Lett.* **6** 181
[17] Barnaby H J, McLain M L, Esqueda I S and Xiao Jie C 2009 *IEEE Trans. Circuits Syst. I, Reg. Papers* **56** 1870
[18] Xu J, Ma Z, Li H, Song Y, Zhang L and Lu B 2018 *IEEE Trans. Semiconduct. Manufact.* **31** 183
[19] Song Y, Zhang G, Cai X, Dou B, Wang Z, Liu Y, Zhou H, Zhong L, Dai G, Zuo X and Wei S H 2022 *Small* **18** e2107516
[20] Chen X J, Barnaby H J, Vermeire B, Holbert K, Wright D, Pease R L, Dunham G, Platteter D G, Seiler J, McClure S and Adell P 2007 *IEEE Trans. Nucl. Sci.* **54** 1913
[21] Chatzikyriakou E, Potter K, Redman-White W and De Groot C H 2017 *Nucl. Instr. Meth. B* **393** 39
[22] Pease R L, Adell P C, Rax B G, Chen X J, Barnaby H J, Holbert K E and Hjalmarson H P 2008 *IEEE Trans. Nucl. Sci.* **55** 3169
[23] Pershenkov V, Bakerenkov A, Rodin A, Felitsyn V, Zhukov A, Telets V and Belyakov V 2020 *Facta universitatis-series: Electronics and Energetics* **33** 303
[24] Srour J R and Mcgarrity J M 1988 *Proc. IEEE* **76** 1443
[25] Esqueda I S, Barnaby H J, Adell P C, Rax B G, Hjalmarson H P, McLain M L and Pease R L 2011 *IEEE Trans. Nucl. Sci.* **58** 2945
[26] Lu Z Y, Nicklaw C J, Fleetwood D M, Schrimpf R D and Pantelides S T 2002 *Phys. Rev. Lett.* **89** 285505
[27] Rowsey N L, Law M E, Schrimpf R D, Fleetwood D M, Tuttle B R and Pantelides S T 2011 *IEEE Trans. Nucl. Sci.* **59** 51
[28] Blöchl P E 2000 *Phys. Rev. B* **62** 6158
[29] Rowsey N L, Law M E, Schrimpf R D, Fleetwood D M, Tuttle B R and Pantelides S T 2011 *IEEE Trans. Nucl. Sci.* **58** 2937
[30] Devine R A B, Mathiot D, Warren W L, Fleetwood D M and Aspar B 1993 *Appl. Phys. Lett.* **63** 2926
[31] Rashkeev S N, Fleetwood D M, Schrimpf R D and Pantelides S T 2001 *Phys. Rev. Lett.* **87** 165506
[32] Huang Q and Jiang J 2019 *Prog. Nucl. Energy* **114** 105
[33] Tuttle B R and Pantelides S T 2009 *Phys. Rev. B* **79** 115206
[34] Chen X J, Barnaby H J, Adell P, Pease R L, Vermeire B and Holbert K E 2009 *IEEE Trans. Nucl. Sci.* **56** 3196
[35] Jafari H, Feghhi S A H and Boorboor S 2015 *Radiat. Meas.* **73** 69
[36] Xu K K 2021 *J. Micromech. Microeng.* **31** 054001
[37] Sills R B and Cai W 2014 *Model. Simul. Mater. Sci. Eng.* **22** 025003
[38] Winokur P S and Boesch H E 1980 *IEEE Trans. Nucl. Sci.* **27** 1647